American Mineralogist, Volume 96, pages 1171–1181, 2011

Identification and characterization of nanosized tripuhyite in soil near Sb mine tailings

Satoshi Mitsunobu,[1,*] Yoshio Takahashi,[2,3] Satoshi Utsunomiya,[4] Matthew A. Marcus,[5] Yasuko Terada,[6] Takeru Iwamura,[1] and Masahiro Sakata[1]

[1]Institute for Environmental Sciences, University of Shizuoka, 52-1 Yada, Suruga-ku, Shizuoka 422-8526, Japan
[2]Department of Earth and Planetary Systems Science, Graduate School of Science, Hiroshima University, 1-3-1 Kagamiyama, Higashi-Hiroshima, Hiroshima 739-8526, Japan
[3]Laboratory for Multiple Isotope Research for Astro- and Geochemical Evolution (MIRAGE), Hiroshima University, 1-3-1 Kagamiyama, Higashi-Hiroshima, Hiroshima 739-8526, Japan
[4]Department of Chemistry, Kyushu University, 6-10-1 Hakozaki, Higashi-ku, Fukuoka 812-8581, Japan
[5]Advanced Light Source, Lawrence Berkeley National Laboratory, One Cyclotron Road, Berkeley, California 94720, U.S.A.
[6]SPring-8, Japan Synchrotron Radiation Research Institute (JASRI), 1-1-1 Kouto, Sayo-cho, Sayo-gun, Hyogo 679-5158, Japan

Abstract

In soil near tailings from an antimony (Sb) mine, we found micro-grains coated with an antimony-rich layer. These grains were characterized in detail using multiple advanced analytical techniques such as micro-X-ray absorption near edge structure (μ-XANES), micro-extended X-ray absorption fine structure (μ-EXAFS), micro-X-ray diffraction (μ-XRD), transmission electron microscope (TEM), and electron probe microanalysis (EPMA). The EPMA showed that one soil grain (grain A) locally accumulated a large amount of Sb in the secondary phases (40–61 wt% Sb_2O_5) with significant Fe (20–28 wt% Fe_2O_3). The spatial distribution of Sb in the grain was similar to that of iron. Both Fe μ-XANES and μ-XRD of the Sb hot spots in grain A consistently showed that the secondary products were dominantly composed of ferric antimonate, tripuhyite ($FeSbO_4$). Fits to the Sb *K*-edge μ-EXAFS of this phase showed second-neighbor coordination numbers ~30% smaller than in bulk tripuhyite, indicating that the tripuhyite included in grain A is nanoparticulate and/or has a high structural disorder. The TEM analysis suggests that the particle size of tripuhyite in grain A was around 10 nm, which is consistent with the size range indicated by μ-XRD and μ-EXAFS. This is the first report showing tripuhyite with nanocrystallinity in natural soil to date.

Keywords: Antimony, tripuhyite, micro-XAFS, micro-XRD, HRTEM

Introduction

Antimony (Sb) is the ninth most mined metal for industrial uses worldwide (Krachler et al. 2001; Filella et al. 2002). It is frequently used as flame retardant, catalyst in plastics, pigment in paints, additive in glassware and ceramics, and alloys for ammunition (Krachler et al. 2001), though Sb and its compounds are considered as pollutants of priority interest (Filella et al. 2002 and references therein). Although the natural abundance of Sb is generally low in soils and sediments (<1 mg/kg) and in fresh water (10^{-3} to 10^{-6} mg/L) (Filella et al. 2002), elevated concentrations of Sb in both soil and water are reported in Sb-contaminated locations, especially in the vicinity of mines and smelters, shooting ranges, and along roads bearing dust from brake pads and tires (Flynn et al. 2003; Furuta et al. 2005; Scheinost et al. 2006; Mitsunobu et al. 2006). However, many questions remain regarding the fate and transport of Sb in aquatic environments (Filella et al. 2002). Oxidation states of Sb most frequently observed in the environment are Sb(III) and Sb(V). In oxic environments, Sb(V) species predominantly occur as $Sb(OH)_6^-$ and are more soluble in water (Filella et al. 2002; Oorts et al. 2008; Mitsunobu et al. 2009). Sb(III) predominates as $Sb(OH)_3^0$ in aqueous solutions and is more stable under anoxic conditions (Filella et al. 2002; Oorts et al. 2008).

Controls on Sb mobility include sorption and incorporation into mineral phases. Iron and Mn hydroxides play an important role in controlling Sb behavior in natural aquatic environments (Crecelius et al. 1975; Brannon and Patrick 1985; Chen et al. 2003; Casiot et al. 2007). Recent studies have suggested that Sb is strongly associated with Fe(III) hydroxides in soils and sediments based on direct evidence using extended X-ray absorption fine structure (EXAFS) spectroscopy (Takaoka et al. 2005; Scheinost et al. 2006; Mitsunobu et al. 2006; Ackermann et al. 2009). Similar findings for the strong preference of Sb binding to Fe(III) hydroxides have been confirmed by lab-based sorption studies of Sb on natural sorbents (Thanabalasingam and Pickering 1990; Leuz et al. 2006; Mitsunobu et al. 2010). Thus, the association with Fe(III) (hydr)oxides can control the mobility of Sb in aquatic environment. However, there are many uncertainties in the formation mechanism, mineralogical structure, and particle size of the Sb-associated Fe (hydr)oxides. These factors largely influence the phase stability and transport of Sb in environment.

Recently, we found micro-scale grains that have accumulated

* E-mail: mitunobu@u-shizuoka-ken.ac.jp

0003-004X/11/0007–1171$05.00/DOI: 10.2138/am.2011.3651

significant amounts of Sb in contaminated soil near antimony-bearing mine tailings. The micro-scale analyses of these soil grains show that they locally contain more than 10 wt% Sb_2O_5 as well as significant iron. In this study, we determined the mineral phase and structure of the soil products, which can elucidate the mechanism of Sb accumulation in soil grains and the effect of Fe phases on Sb accumulation. This study also provides valuable insights on Fe-based water treatment methods for Sb removal in effluents. To analyze the micro-scale distribution and speciation of Sb in natural soil samples, we used multiple analytical methods; Sb and Fe micro-X-ray absorption near edge structure (μ-XANES), Sb micro-extended X-ray absorption fine structure (μ-EXAFS), micro-X-ray diffraction (μ-XRD), transmission electron microscopy (TEM), and electron probe microanalysis (EPMA). These methods provide information on the mineralogy, elemental distribution, chemical form and coordination environments of Sb and Fe, as well as particle size.

Samples and experimental methods

Ichinokawa soil sample

Natural soil samples were collected near the Ichinokawa mine tailings (N33°53′, E133°12′) in Ehime prefecture, Japan. (See Supplementary Fig. 1[1] for map and other data in Supplementary Table 1[1].) The mine was formerly one of the largest stibnite (Sb_2S_3) mines in the world (Bancroft 1988) although is no longer in operation. The sample site was located about 10–50 m downhill of the mine-pits and tailings within a soil horizon covered by 20 cm of water. The mine wastewater flowed steadily and year round from the mine-pits and into the soil and, as such, the soil was heavily contaminated with Sb, As, and heavy metals. Bedrock is found at a depth of about 15 cm beneath the soil horizon at the sampling site. Surface soil samples (~10 cm) under the water layer were collected using a plastic spatula. The pH of the soil (ranging from 7.6 to 7.7) was measured in situ by inserting a glass electrode into the soil. The collected soil sample was immediately sealed in a polystyrene bottle and kept at 4 °C during transport to the laboratory where the soil sample was immediately passed through a 500 μm stainless steel sieve to remove large organic particles and gravel fractions. To minimize reactions in the soil sample such as transformation of metastable nanoparticles, sieving was done at about 0–5 °C and the sample was stored at –20 °C until analysis. Bulk concentrations of major elements in the collected surface soil were measured by X-ray fluorescence spectrometry (XRF; Rigaku ZSX-101e). Antimony and arsenic concentrations in the soil sample were determined using the standard addition method by XRF. In addition, mineral compositions in bulk soil were analyzed by powder X-ray diffraction (XRD; Rigaku Multiflex) with a Cu$K\alpha$ radiation source (λ = 1.54056 Å).

Ichinokawa soil sample thin section preparation

A thin section of the soil sample was prepared for micro-scale analyses, namely μ-XAFS, μ-XRD, and EPMA. The soil sample was air-dried in a N_2-purged glovebox to prevent transformation to unstable materials. A few grams of the soil was dispersed in a high-purity resin (Eposet, Maruto Co.), glued onto a glass plate with a wax product, and polished with abrasive (α-Al_2O_3) paper. The epoxy-resin was selected in this study because it was reported to be inert toward metal(loid)s reactivity (Manceau et al. 2002) and is often used for embedding natural samples in similar μ-XAFS studies (Reguer et al. 2005; Takahashi et al. 2007; Endo et al. 2008). The other surface of the sample was polished and the resulting 40 μm thick thin section was removed from the glass plate by dissolving the wax (Takahashi et al. 2007). Finally, the double-polished thin section was attached to a plastic plate with a hole in the center for Sb and Fe μ-XAFS, μ-XRD, and EPMA analyses, such that the X-ray beam only irradiated the sample and not the plastic plate.

Preparation of reference materials for XAFS

The iron reference materials used for XAFS included ferrihydrite, goethite, lepidocrocite, hematite, and magnetite were prepared according to Schwertmann and Cornell (2000). Pyrite and siderite were also used as reference standards and purchased from Hori Mineralogy, Japan. Mineralogical verifications were conducted using powder XRD with Cu$K\alpha$ radiation.

Tripuhyite ($FeSbO_4$) was synthesized following a method presented by Basso et al. (2003). A mixture of Sb_2O_3 and $FeSO_4{\cdot}7H_2O$ (Sb/Fe molar ratio = 1) was heated at 1273 K for 20 h in air. The phase identity of synthesized tripuhyite was confirmed by normal and synchrotron powder XRD; the patterns were consistent with published data of pure tripuhyite. Micrometer-scale observations of the solid were completed by scanning electron microscopy (SEM; JEOL JSM-5310LV) and the images showed that particle size of the synthesized tripuhyite is predominantly micrometer-scale.

μ-XAFS analyses

Antimony *K*-edge μ-XAFS experiments were performed at BL37XU at SPring-8, a third-generation synchrotron facility in Hyogo, Japan (Terada et al. 2004). The incident beam was monochromated with a Si(111) double-crystal monochromator and focused to 0.9 (V) μm ×1.3 (H) μm at the sample position by a Kirkpatrick-Baez (K-B) mirror system (Suzuki et al. 2007). Pure reference compounds and the soil samples were analyzed in transmission and fluorescence detection modes at the Sb absorption *K*-edge. The thin section sample was fixed on a sample holder oriented at 10° to the beam. The fluorescence X-ray spectrum of Sb was measured by Si(Li)-SSD (SEIKO EG&G). Energy calibration was conducted using a reference sample of metallic Sb by defining the energy of 30.491 keV at the inflection point on the white line of the Sb *K*-edge.

The XAFS data for Sb was analyzed by REX2000 (Rigaku Co.). The theoretical phase shift and amplitude functions in simulation of Sb EXAFS were extracted from FEFF 7.0 (Zabinsky et al. 1995), in which the structure of tripuhyite ($FeSbO_4$) was used as an input data to run FEFF for Sb-O and Sb-Fe shells (Berlepsch et al. 2003). The Sb EXAFS oscillation was extracted from the original spectrum by a spline smoothing method. E_0 was set at the edge inflection point for all the samples studied. The Fourier transformation of the $k^3\chi(k)$ EXAFS function from k space to r space was performed in a range 2.2–12.0 $Å^{-1}$ for the sample to obtain a radial structural function (RSF). The inversely Fourier filtered data were analyzed with a usual curve fitting method. The S_0^2 factor was fixed at 1 for the theoretical calculation by FEFF 7.0 since model compounds with well-known structure from crystallographic data are not available for the sorbed and coprecipitated species to optimize S_0^2. Final fits were obtained for k-space data using REX2000. The edge inflection point was determined as a maximum of the first derivative. The uncertainty in the analysis was evaluated by the R factor given by Equation 1.

$$R = \sum\left\{k^n\chi_{\text{obs}}(k) - k^n\chi_{\text{cal}}(k)\right\}^2 / \sum\left\{k^n\chi_{\text{obs}}(k)\right\}^2 \quad (1)$$

The phase shifts and amplitude functions extracted from FEFF 7.0 were considered in the simulation using REX2000. FEFF 7.0 was also used to evaluate the importance of the multiple scattering (MS) contribution to the EXAFS spectra of the natural soil sample by evaluating MS in the structure of tripuhyite. As a result, all three-leg and four-leg MS paths with a total length <4.1 Å were considered with smaller errors in the simulation of synthetic tripuhyite and soil samples.

Iron μ-XANES spectra were recorded on the BL-4A beamline of KEK-PF, Tsukuba, Japan, with a Si(111) double-crystal monochromator. The thin section was fixed on a sample holder oriented at 45° to the beam. The beam was focused by K-B optics, and the beam diameter was 5 (V) μm ×5 (H) μm, which translates to 5 (V) μm ×7 (H) μm on the sample. The Fe μ-XANES spectra of reference materials (pyrite, siderite, magnetite, hematite, lepidocrocite, ferrihydrite, goethite, and tripuhyite) and the soil sample were measured in transmission and fluorescence modes, respectively. Fluorescence X-rays were detected by a Ge-SSD. The energy calibration for Fe was performed using the pre-edge peak maximum of hematite fixed at 7.113 keV. The XANES data was also analyzed by REX2000.

Check of radiation-induced alteration in Sb μ-XAFS

Antimony *K*-edge μ-XAFS measurements were conducted using high energy and brilliant X-ray microbeam. To test the effects of possible radiation-induced alteration of Sb in soil samples, we collected several successive scans of $KSb^{V}(OH)_6$, $Sb^{III}_2O_3$, and an Sb hot spot in the soil grain having a similar composition to point studied. Three successive scans (10 min for each) of each sample were collected. Shifts in the E_0 position were not observed during the successive

[1] Deposit item AM-11-035, Supplementary Figure 1 and Table 1. Deposit items are available two ways: For a paper copy contact the Business Office of the Mineralogical Society of America (see inside front cover of recent issue) for price information. For an electronic copy visit the MSA web site at http://www.minsocam.org, go to the *American Mineralogist* Contents, find the table of contents for the specific volume/issue wanted, and then click on the deposit link there.

scans of all samples (Fig. 1). These results show that there was no beam-induced oxidation or reduction of Sb in the samples during 30 min radiation. To avoid radiation damage, the duration of each scan was limited to less than 30 min for an Sb μ-XAFS spectrum on each point in this study and only one spectrum was collected at each point. Endo et al. (2008) conducted As *K*-edge μ-EXAFS measurement of natural sediment samples using the same beamline, BL37XU, in SPring-8, and showed that no apparent photo-alteration was observed under similar experimental conditions.

μ-XRD analyses

μ-XRD pattern of a soil grain was collected at Beamline 10.3.2 of the Advanced Light Source, at Lawrence Berkeley National Laboratory. The pattern was recorded in transmission mode with a 1024 × 1024 pixel CCD camera at 17 keV for 5 min with a beam focused to 6.2 (V) μm × 15.1 (H) μm. The data were converted to *d*-spacings using an α-Al_2O_3 standard spectrum and the FIT2D software (Hammersley 1998).

Chemical analyses by EPMA

Following the X-ray analyses, the microscopic elemental distribution and morphology in the soil were characterized by EPMA (JXA-8200, JEOL). Quantitative EPMA were performed by wavelength-dispersive spectrometry (WDS) operated at 15 kV with a beam current of 15 nA. The beam diameter was set to 2 × 2 μm. The count time was 20 s for each element except for Sb (30 s) and S (10 s), and raw data corrections were made using the ZAF method (i.e., correction for atomic number, absorption, and fluorescence effects in X-ray microanalysis). The following X-ray lines and standards were used: Si*K*α (jadeite), Al*K*α (synthetic Al_2O_3), Fe*K*α (synthetic Fe_2O_3), Mn*K*α (synthetic MnO), S*K*α (chalcopyrite), P*K*α (synthetic InP), Ca*K*α (wollastonite), Sb*L*α (stibnite), and As*L*α (synthetic As metal). The elemental distribution map for soil products (Fig. 2) was produced using backscattered electron (BSE) micrographs and X-rays of each element in EPMA operated under the following conditions: accelerating voltage 15 kV, beam current 30 nA, counting time 0.4 s/point, and beam size 1 μm × 1 μm.

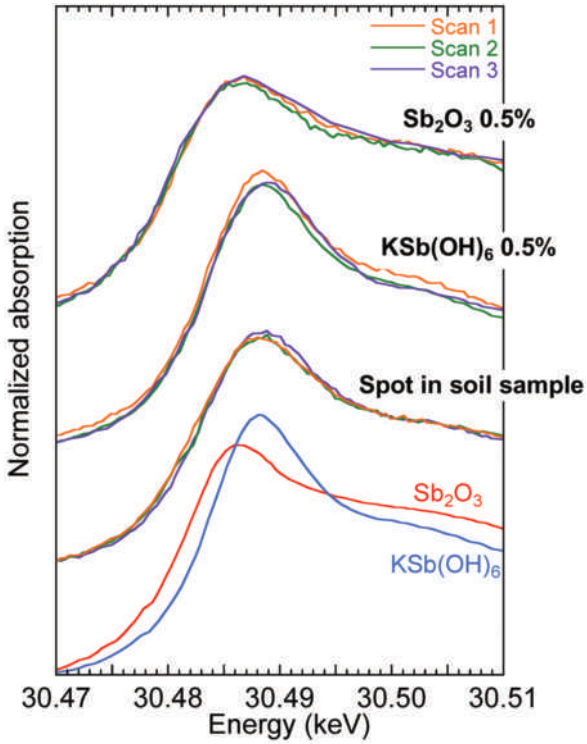

FIGURE 1. Antimony *K*-edge μ-XANES spectra for check of radiation-induced alteration. Samples are 0.5 wt% Sb_2O_3 + 0.5 wt% $KSb(OH)_6$ in BN pellet (two spectra at the bottom) and a spot in soil sample used in present study (Sb abundance around the spot determined by EPMA: 10–12 wt% Sb_2O_5, initial Sb oxidation states of the spot: Sb(V) 100 ± 5%). (Color online.)

TEM analyses

The TEM and analytical electron microscopy (AEM) were performed using a FEI, TECNAI-20 with an accelerating voltage of 200 kV. The spherical aberration coefficient, C_S, was 1.2 mm. The TEM specimen was prepared by detecting the material from the Sb hot spots. Small amounts of the hot spot were dispersed in methanol in an ultrasonic bath (Utsunomiya et al. 2009). A drop of the resulting suspension was placed on a perforated carbon mesh supported by a Cu-grid.

RESULTS AND DISCUSSION

Elemental distribution and chemical analyses

The bulk concentrations of major element oxides measured by XRF are summarized in Table 1. The soil was heavily contaminated with Sb (bulk Sb concentration in soil: ~1 wt%; Table 1). The soil toxicity threshold (half maximal effective concentration) identified in laboratory toxicity tests ranges from 0.5 to 8 mmol Sb kg^{-1} depending on the endpoint, soil, and Sb form tested (Hammel et al. 1998; He and Yang 1999; Murata et al. 2005; Kuperman et al. 2006). Thus, Sb concentration in the soil (1 wt% = 82 mmol Sb kg^{-1}) was at least 10× higher than the soil toxicity threshold. In addition, based on the XRD and EPMA analyses, stibnite was not present in the soil samples studied at levels exceeding detection limits. The major minerals in the soil were quartz, albite, and phyllosilicates such as kaolinite, mica, and illite.

EPMA of the thin section of soil was conducted to gain information on local elemental distributions, the spatial relationship of phases, and mineralogical compositions in the soil at the micro-scale. Figure 2 shows backscattered electron images (BSEs) and element distribution maps for Sb, Fe, and Si of soil grains A–D in the Ichinokawa soil. Quantitative EPMA reveals detrital silicate minerals such as quartz, biotite, and albite. The BSE images revealed that quartz and biotite in grain A were cemented by a matrix of secondary products. In grains B–D, secondary products (2–15 μm thick) coated the surfaces of silicate minerals. The secondary products in all grains existed as discrete particles and fine-grained agglomerations, indicating that these products were authigenic minerals precipitated during or after deposition (Paktunc et al. 2003, 2004; Fandeur et al. 2009). The elemental maps for all grains consistently showed that most of Sb accumulated into the secondary products (Fig. 2) and that the distributions of Sb were similar to those of Fe, indicating that Sb is associated with secondary Fe phases. Ackermann et al. (2009) have reported a similar accumulation of Sb in secondary products bearing Fe in contaminated soil around a shooting range using micro-scale analysis. In addition, previous studies also showed that Sb has a strong preference for Fe oxide phases [e.g., Fe(III) hydroxides] in soils under oxidizing conditions (Chen et al. 2003; Scheinost et al. 2006). These reports are consistent with our findings.

Table 2 shows the chemical compositions of the secondary products (=Sb hot spots) for all soil grains based on quantitative single-point analyses. The wt% totals are low (within a range of

TABLE 1. Bulk concentrations of various elements in the Ichinokawa soil sample used in this study

Sb (mg/kg)	As (mg/kg)	SiO_2 (wt%)	TiO_2 (wt%)	Al_2O_3 (wt%)	Fe_2O_3* (wt%)	MnO† (wt%)	MgO (wt%)	CaO (wt%)	Na_2O (wt%)	K_2O (wt%)	P_2O_5 (wt%)
9955	1460	55.34	0.54	12.81	6.52	0.71	1.09	0.79	1.20	2.37	0.12

* Total iron as Fe_2O_3.
† Total manganese as MnO.

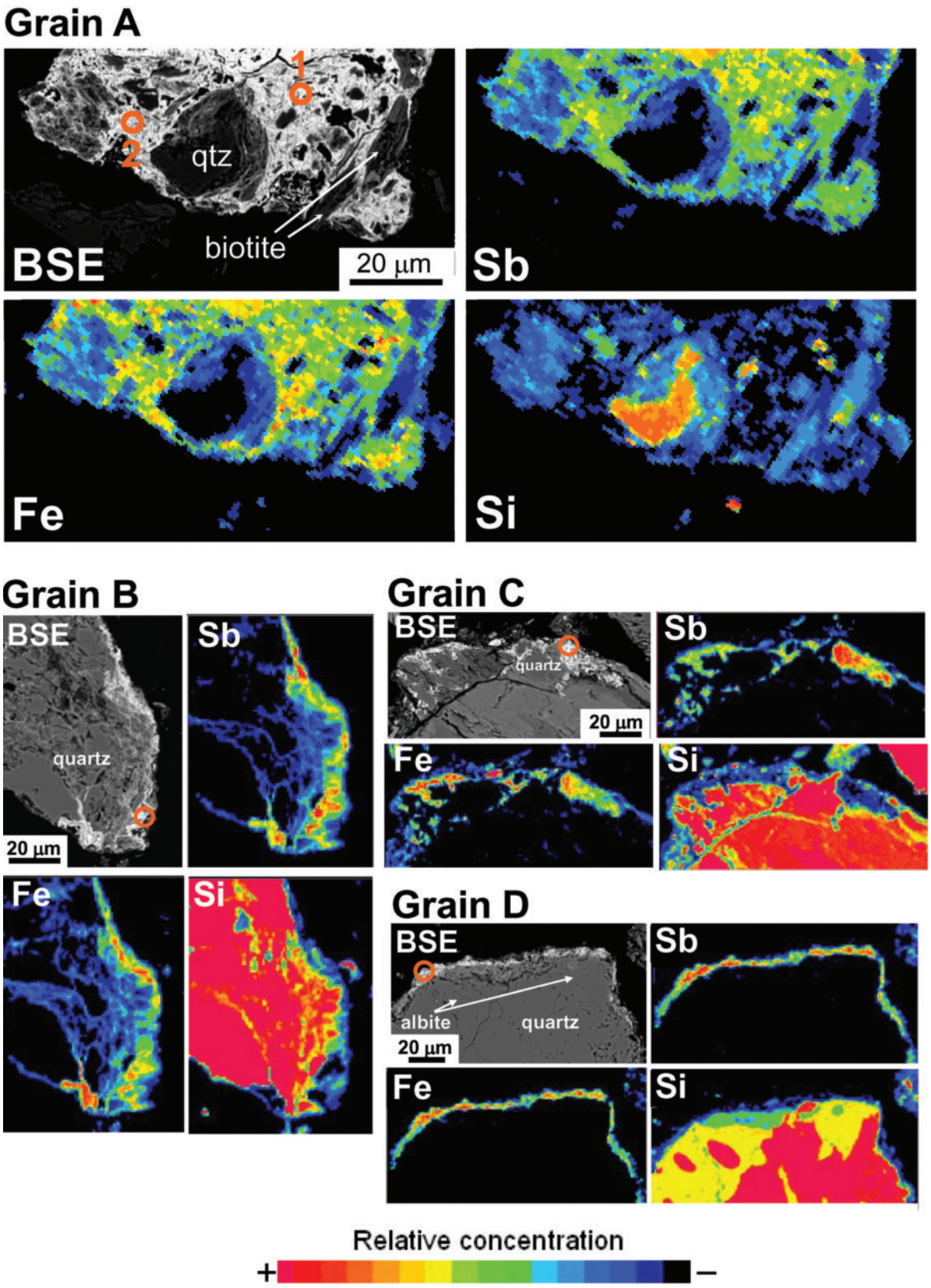

FIGURE 2. Backscattered electron photographs (BSE) and elemental distribution maps for Sb, Fe, and Si of soil grains A–D in the Ichinokawa soil. In grain A, the orange circles in the BSE indicate two spots (spots 1 and 2) where Fe μ-XANES, μ-XRD, and Sb μ-XAFS were measured. For grains B–D, an orange circle in each grain shows the points where Fe μ-XANES was measured. (Color online.)

70–80 wt%) and are likely caused by various factors such as the porosity of the matrix, the presence of water in hydrated minerals, high concentration of light elements (C, H, N), and the high relief of the sample in thin section (Abreu and Brearley 2010). Low totals are often found in secondary products contained in soils and mine tailings (Majzlan et al. 2007; Paktunc et al. 2004; Ackermann et al. 2009). Iron is the most abundant component in the Sb hot spots of grains B–D (18–57 wt% as Fe_2O_3); the rims also contain a high proportion of Sb_2O_5 (from 7 to 33 wt%).

In contrast, the secondary products of grain A accumulated higher Sb than grains B–D. The Sb abundances in the products of grain A are 40–61 wt% Sb_2O_5 and Fe concentrations range from 20–28 wt% Fe_2O_3. Thus, Sb is the most abundant element in the secondary products in wt% units in grain A. We carefully analyzed the other soil grains with Sb hot spots (more than 20 grains) in the soil by EPMA, and the results showed that grain A had the highest Sb among all grains. Ackermann et al. (2009) reported that 2–7 wt% Sb_2O_5 was locally contained in secondary products bearing Fe in natural soil near a shooting range. In addition, Majzlan et al. (2007) found Fe-bearing materials near Sb mine tailings contained ~30 wt% Sb_2O_5 in the solids. Thus, the secondary products of grain A are more Sb-rich when compared to previous reports. Previous studies have shown that the incorporation capacity of a metal(loid) into solid [e.g., Fe(III) hydroxides] in coprecipitation is generally larger than that in adsorption (Pactunc et al. 2003; Fuller et al. 1993). This indicates that the major Sb in grain A may be a coprecipitated species and/or an Sb-bearing mineral phase rather than an adsorbed species.

Therefore, we selected grain A as the main target sample in the present study and characterized the grain in detail using multiple methods to obtain information on the mineralogical and chemical species. The investigations lead to an understanding of the mechanism of Sb accumulation and enhancement of Sb incorporation into nanosized solids such as Fe hydroxides.

Iron μ-XANES analyses

We conducted Fe μ-XANES analyses to determine the Fe phases in the Sb hot spots in grain A, since Fe μ-XANES can be used to distinguish the mineralogical phase of Fe (O'Day et al. 2004). EPMA showed that grain A has high Sb and Fe abundances and lesser amounts of elements such as Si, S, P, Al, and Mn (Table 2). The results indicate that the presence of silicate, sulfide, phosphate, and Al and Mn oxides can be eliminated as possible Sb-hosting phases in grain A. Instead, these parts may be composed of Fe hydroxides and/or other phases bearing Sb and Fe. Thus, we selected typical soil Fe (hydr)oxides (ferrihydrite, goethite, lepidocrocite, magnetite, and hematite) and Fe-Sb oxide (tripuhyite) as reference materials for the Fe μ-XANES. Iron μ-XANES features of the points in grain A (spots 1 and 2 in Fig. 2) are similar to those of Fe(III) hydroxides and significantly differ from other Fe species including Fe(II). The spots analyzed were in approximately the same areas as those analyzed by μ-XRD and Sb μ-XAFS. Two peaks around the edge of the Fe μ-XANES spectra were observed in spots 1 and 2, and the positions of peaks were similar to those of tripuhyite spectrum (Figs. 3a and 3b). Fitting of Fe μ-XANES was carried out to determine the abundance of Fe phases in grain A. The results show that the Sb hot spots contain 86–87% tripuhyite and 13–14% fer-

TABLE 2. Representative electron microprobe analyses of Sb hot spots of grains A–D in wt%

Fe_2O_3*	Sb_2O_5†	As_2O_5‡	SiO_2	MnO§	CaO	Al_2O_3	SO_3‖	P_2O_5	Total
Spots in grain A									
23.65	60.53	0.94	0.90	2.83	1.44	2.78	0.51	0.20	93.76
24.48	59.05	0.98	0.97	2.85	1.09	3.35	0.61	0.24	93.62
23.56	59.11	0.79	1.53	2.94	1.57	3.97	0.47	0.14	94.06
24.21	60.25	0.96	1.16	2.48	1.68	3.29	0.30	0.19	94.51
20.29	49.71	0.78	9.10	2.38	1.50	8.30	0.34	0.21	92.60
24.03	57.86	0.84	1.22	3.04	1.32	3.70	0.33	0.20	92.54
22.47	51.94	0.81	1.59	2.79	1.39	3.55	0.36	0.13	85.02
26.95	47.28	1.19	5.86	2.07	1.56	6.61	0.32	0.15	91.98
23.76	48.45	1.22	5.91	2.14	1.66	5.35	0.18	0.16	88.82
27.72	51.26	1.29	5.31	2.13	1.52	5.51	0.15	0.17	95.06
20.42	39.39	0.54	3.75	1.69	1.83	2.23	0.16	0.15	70.17
27.30	52.05	1.20	5.49	1.80	1.62	5.44	0.22	0.20	95.31
24.12	43.16	1.30	1.33	2.01	0.95	1.24	0.37	0.12	74.58
20.38	40.47	0.85	10.08	1.50	1.33	9.34	0.26	0.19	84.41
25.90	49.17	1.22	1.67	1.64	1.32	1.82	0.14	0.19	83.07
Rim on grain B									
41.03	30.49	3.74	4.87	1.33	1.90	6.71	0.55	1.17	91.78
31.44	23.30	1.33	20.73	0.80	0.80	15.63	0.19	0.57	94.79
36.20	29.80	2.89	4.85	1.39	1.81	6.33	0.56	0.98	84.81
43.71	29.81	3.30	5.54	1.38	1.64	6.87	0.45	1.05	93.76
52.19	22.40	2.75	5.89	1.20	1.15	5.66	0.53	0.88	92.65
55.01	21.28	1.63	6.35	0.99	0.92	4.63	0.47	0.67	91.94
43.11	19.19	1.40	13.54	0.79	0.77	9.66	0.33	0.56	89.35
42.77	18.59	1.47	13.64	0.93	0.92	9.41	0.41	0.63	88.79
41.32	22.32	2.95	8.59	1.09	1.33	8.38	0.44	1.11	87.53
49.57	32.54	2.15	2.82	1.37	1.37	2.26	0.47	0.73	93.29
44.48	26.82	2.28	10.56	1.10	1.03	8.89	0.27	0.58	95.99
48.67	25.33	2.41	2.14	1.18	1.09	1.77	0.54	0.72	83.84
48.91	26.96	1.88	1.57	1.17	1.05	1.82	0.43	0.65	84.43
52.09	18.32	2.47	6.55	1.31	1.23	2.26	0.90	1.07	86.21
57.43	19.29	3.39	2.81	1.28	1.26	3.10	1.00	1.27	90.82
49.74	15.95	2.00	14.79	1.09	1.04	1.77	0.82	0.80	88.01
Rim on grain C									
34.57	23.83	1.47	5.96	0.84	0.64	5.41	0.27	0.27	73.25
32.51	20.45	1.48	4.28	0.74	0.46	4.49	0.28	0.25	64.94
39.84	25.14	1.74	4.60	0.82	0.55	4.37	0.24	0.20	77.50
42.08	25.91	1.51	4.98	0.89	0.57	4.95	0.31	0.24	81.44
40.84	25.88	1.86	3.86	0.89	0.56	4.13	0.23	0.35	78.59
43.97	25.49	1.58	5.70	0.82	0.54	5.27	0.24	0.23	83.85
44.67	26.52	1.83	5.81	0.86	0.63	5.23	0.27	0.32	86.13
45.35	27.78	1.86	5.24	0.91	0.75	5.15	0.28	0.32	87.65
46.68	22.03	1.54	8.29	0.78	0.68	5.99	0.31	0.25	86.55
44.00	18.34	1.52	5.68	0.75	0.63	5.74	0.43	0.26	77.34
45.98	18.26	1.44	4.92	0.81	0.59	5.16	0.43	0.26	77.84
53.39	18.20	1.29	4.95	0.70	0.65	5.10	0.50	0.23	85.00
52.87	18.47	1.60	6.20	0.79	0.64	6.55	0.43	0.28	87.83
42.51	16.35	1.16	7.20	0.63	0.54	6.21	0.46	0.20	75.25
37.05	14.71	1.05	8.76	0.62	0.56	7.30	0.48	0.22	70.74
46.52	18.57	1.34	3.75	0.75	0.63	4.38	0.40	0.20	76.55
Rim on grain D									
37.91	15.23	2.42	9.00	1.32	1.35	9.26	0.55	0.55	77.57
32.33	14.00	2.42	8.92	1.60	1.35	8.44	0.76	0.61	70.43
47.44	19.88	3.00	5.79	1.61	1.64	7.19	0.58	0.69	87.81
27.79	11.74	1.58	25.04	1.02	1.19	11.63	0.53	0.52	81.04
37.39	15.83	2.28	9.92	1.26	1.38	7.75	0.78	0.53	77.12
36.69	15.35	2.46	9.99	1.22	1.42	8.69	0.72	0.73	77.27
17.64	7.19	0.67	35.33	0.69	0.67	22.51	0.25	0.21	85.16
39.84	15.61	1.98	9.29	1.32	1.65	8.49	0.75	0.55	79.47
18.48	7.22	0.60	34.16	0.73	0.75	21.70	0.38	0.21	84.23
27.27	11.65	1.11	22.59	0.99	1.15	14.81	0.54	0.44	80.53
32.13	14.20	1.22	18.21	1.07	1.23	12.51	0.42	0.40	81.39
36.46	16.54	2.23	9.11	1.43	1.22	9.96	0.70	0.52	78.16
36.10	15.07	1.74	15.11	1.47	1.19	10.76	0.66	0.49	82.59
32.52	13.58	1.73	16.50	1.25	0.98	12.70	0.78	0.54	80.58
19.98	9.21	1.25	30.33	0.66	0.60	19.59	0.40	0.31	82.33

Note: Oxidation state of elements, for which multiple oxidation states are known, is assumed.
* Total Fe as Fe_2O_3.
† Total Sb as Sb_2O_5.
‡ Total As as As_2O_5.
§ Total Mn as MnO.
‖ Total S as SO_3.

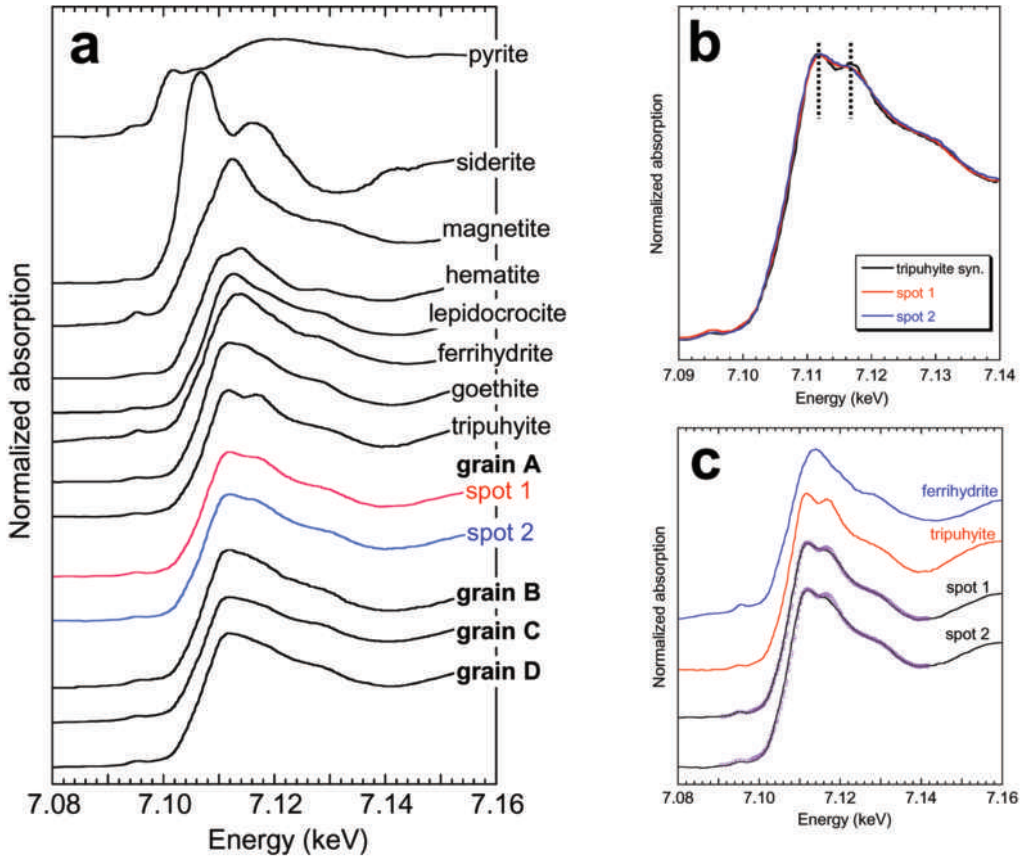

FIGURE 3. (**a**) Normalized Fe *K*-edge μ-XANES spectra of reference materials (pyrite, siderite, magnetite, tripuhyite, ferrihydrite, hematite, lepidocrocite, and goethite) and spots in grains A–D (see Fig. 2). The dilution of the reference materials for XAFS was done using BN and measured in transmission mode. (**b**) Iron *K*-edge μ-XANES spectra of tripuhyite and 2 spots on grain A. In **b**, the dotted lines show the positions of two peaks observed around the edge of synthetic tripuhyite. (**c**) Normalized Fe *K*-edge μ-XANES spectra of reference materials (tripuhyite and ferrihydrite) and two spots in grain A. Fitted spectra are shown by purple dots. The fit of spots in grain A were conducted within a fixed range of 7.090–7.142 keV. (Color online.)

rihydrite (Fig. 3c; Table 2), indicating that tripuhyite dominates as the Fe phase in the Sb hot spots. On the other hand, a Fe_2O_3 vs. Sb_2O_5 plot of each grain (Fig. 4) based on EPMA shows a positive correlation between Fe and Sb ($R = 0.70$). In particular, the molar ratios of Fe/Sb of grain A were around 1, lower than other studied grains which have molar ratios of Fe/Sb above 1 (Fe/Sb values of grain A: 0.79–1.16, grain B: 2.46–6.32, grain C: 2.94–5.94, grain D: 4.40–5.17). Since the theoretical Fe/Sb ratio of the tripuhyite ($FeSbO_4$) is 1 (Berlepsch et al. 2003) and the ratio is unique to tripuhyite among oxides bearing Fe and Sb, the results of EPMA and Fe μ-XANES suggest that Sb hot spots in grain A are dominantly comprised of tripuhyite.

μ-XRD analyses

Figure 5a shows the two-dimensional μ-XRD patterns of Sb hot spots in grain A and in synthetic tripuhyite. Diffuse rings were observed in spots 1–4 in Figure 5a, which corresponds to the three brightest reflections of tripuhyite (110, 101, and 211 planes). Thus, the Sb hot spots in grain A mainly contains tripuhyite, which is consistent with Fe μ-XANES and EPMA.

One-dimensional patterns in Figure 5b show that the peaks corresponding to tripuhyite are much broader than in the synthetic mineral, the particle size of which is micrometer-scale based on

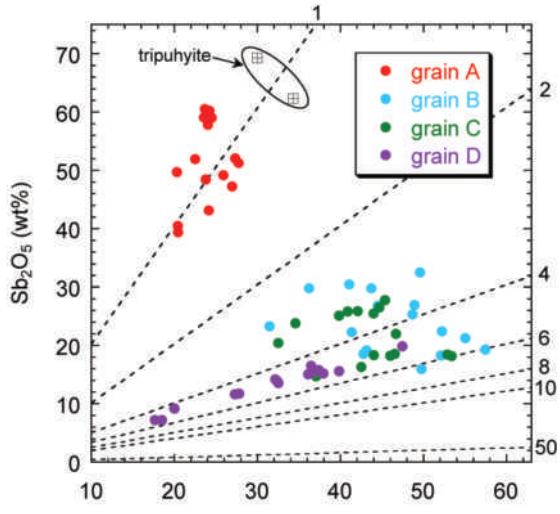

FIGURE 4. Variation of wt% Sb as a function of wt% Fe_2O_3 in grains A–D and tripuhyite ($FeSbO_4$) from quantitative EPMA. Chemical components of tripuhyite are in the data reported by Basso et al. (2003) and Berrepsch et al. (2003). Dotted lines are Fe/Sb molar ratios. Detailed chemical components in each grain are shown in Table 2. (Color online.)

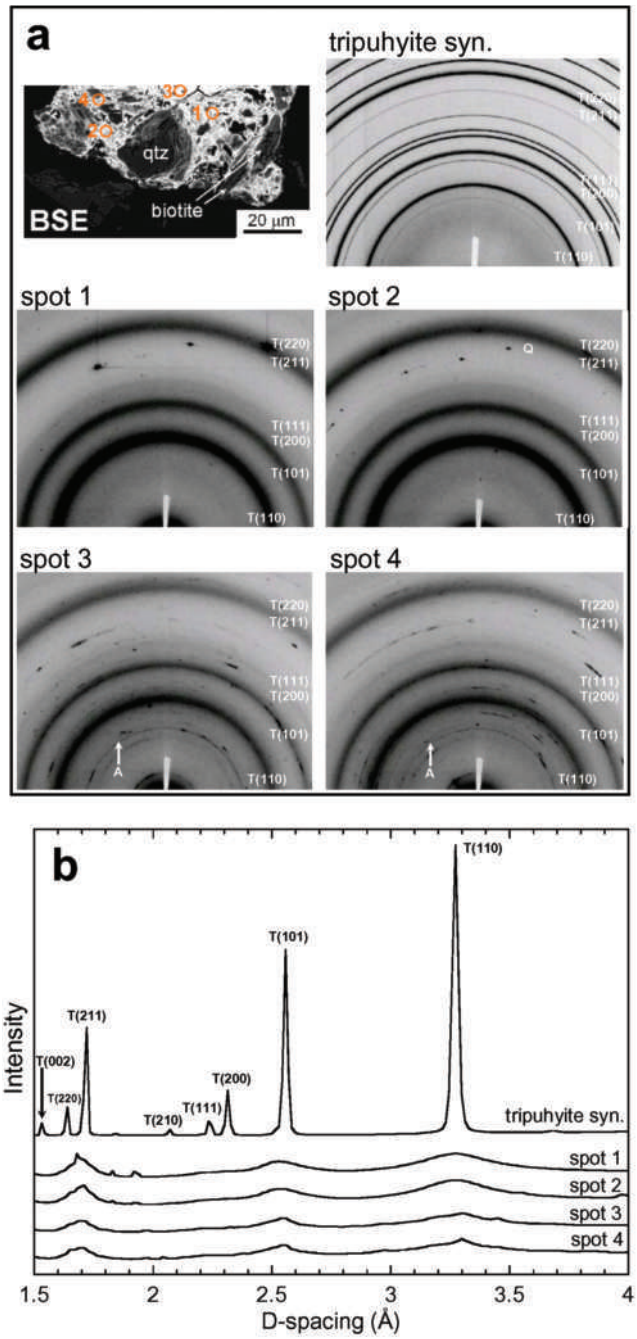

FIGURE 5. (**a**) Two-dimensional μ-XRD patterns and (**b**) one-dimensional μ-XRD patterns of synthetic tripuhyite and 4 spots on grain A. In **a**, Q and A stand for quartz and anatase, respectively. (Color online.)

SEM analyses. The broad peaks observed for the natural sample can be the result of small particle size and can be quantified by the Scherrer relation (Warren 1968). Previous studies have also showed that the peak shapes of nanosized solids have relatively broad patterns (Waychunas 2001). Moreover, there also appears to be an effect of decreasing degree of disorder in the structure (Waychunas et al. 2005). Therefore, it is anticipated that the tripuhyite in the Sb hot spots have nanoscale particle size and/or are highly disordered.

In addition to the tripuhyite peaks, other rings and spots were observed in grain A. These indicate the presence of detrital silicate minerals such as anatase, which is consistent with higher abundances of Si and Al in the EPMA of grain A (Table 2). Some rings and spots in Figure 5a have been unidentified but are not derived from sulfide minerals such as stibnite and pyrite.

Antimony μ-XANES and μ-EXAFS analyses

Information on the chemical species of Sb and the local environment around Sb in the grain A is provided by Sb μ-XANES and EXAFS analyses. Figure 6 shows Sb μ-XANES of 2 spots in grain A and reference material [Sb_2O_3, $KSb(OH)_6$, and synthesized tripuhyite]. The position of the XANES peak can be used to distinguish the oxidation states of Sb (Fawcett et al. 2009). The Sb absorption edge of both spots in grain A was identical to that of $KSb(OH)_6$ and synthesized tripuhyite, indicating that Sb in the samples is predominantly Sb(V).

The μ-EXAFS spectra of Sb in grain A and synthetic tripuhyite as a model compound are shown in Figure 7. We assume that the μ-EXAFS spectra of spots 1 and 2 predominantly result from Sb in tripuhyite because the tripuhyite abundances are about 90% in both spots without other phases containing Sb (Fig. 3; Table 3). The μ-EXAFS spectra for grain A and tripuhyite have essentially same phase and line shape, but they are significantly different in their fine structures and amplitudes. In the μ-EXAFS of synthesized tripuhyite, several peaks are observed at k = 5, 7, 9, and 11 Å^{-1} (arrows in Fig. 7a) on the main oscillation structure. However, the intensities of these peaks are overall attenuated in the spectra of both spots 1 and 2 (in particular, peaks at k = 5 and 7 Å^{-1} are not obvious in their spectra).

In both Fourier transformations (FTs) of the μ-EXAFS spectra for synthetic tripuhyite and natural samples, the first pronounced peak corresponding to O atom coordination was observed at R+ΔR = 1.5 Å (phase shift uncorrected) in Figure 7b and its intensity and position did not change in the FTs. Based on the fit of theoretical to experimental spectra, the first peak is composed of approximately six O atoms at an average distance of 1.97–1.98 Å from the central atom (Table 4). In the FT of synthetic tripuhyite, three peaks at R+ΔR = 2.2–3.8 Å corresponding to contributions from Sb-Fe, Sb-Sb, and multiple scattering (MS) shells were also isolated and fitted (Fig. 7b). Thus, the fitting was improved by considering the MS paths in addition to Sb-Fe and Sb-Sb shells with two linkage types, because Sb in tripuhyite is surrounded by one Fe and one Sb atom with edge-sharing and four Fe and four Sb atoms with corner-sharing links. The fitted distances for the synthetic tripuhyite are 3.07 and 3.62 Å for Sb-Fe shells and 3.09 and 3.60 Å for Sb-Sb shells. These values agree with published data considering fitting errors (Berlepsch et al. 2003; Scheinost et al. 2006; Table 4).

In FTs of spots in grain A, three peaks at R+ΔR = 2.2–3.8 Å were also isolated and fitted in a similar fashion to synthetic tripuhyite (Fig. 7b); the distances are 3.06–3.07 and 3.59–3.60 Å for Sb-Fe links and 3.07 and 3.60 Å for Sb-Sb links. On the other hand, the intensities of Sb-Sb and Sb-Fe shells in FTs of spots 1

TABLE 3. Fitting results of Fe μ-XANES in grain A

	Tripuhyite (%)	Ferrihyrrite (%)	Fitting error (%)
Spot 1	86	14	±5
Spot 2	87	13	±7

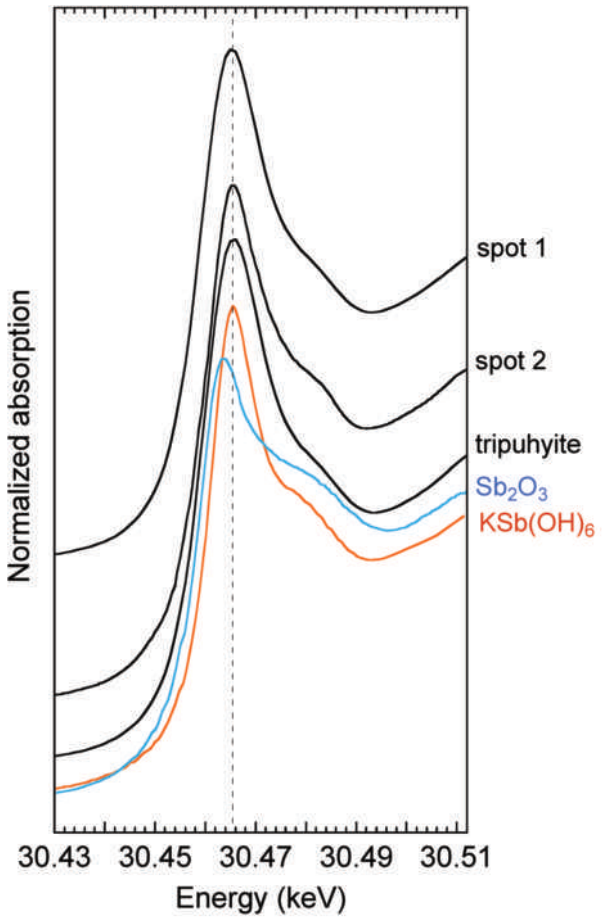

FIGURE 6. Normalized Sb *K*-edge μ-XANES of reference materials [Sb_2O_3, $KSb(OH)_6$, and synthetic tripuhyite] and Sb hot spots in grain A in the Ichinokawa soil. The spots of grain A correspond to the orange circles (spots 1 and 2) in the BSE images in Figure 2a. A dotted line indicates the peak-top energy of $KSb(OH)_6$. (Color online.)

and 2 are significantly smaller than those of synthetic tripuhyite, which implies lower coordination numbers (CNs) of the links than in synthetic tripuhyite. In fact, fitted CNs of the Sb-Fe and Sb-Sb links decreased compared with those of synthetic tripuhyite regardless of the linkage types (e.g., edge- and corner-sharing links in Table 4). In addition, the decrease of CNs of next neighbor atoms may also indicate the attenuation of specific peak intensities in μ-EXAFS observed in spots of grain A (Fig. 7a; above mentioned), because these specific peaks are due to the contributions of Sb-Sb, Sb-Fe, and MS shells for tripuhyite based on the Fourier filtered Sb-Fe and Sb-Fe contributions to the μ-EXAFS (Fig. 8).

The decrease in next neighbor CNs indicate the following scenarios: (1) reduced CNs from small particle size (size effect);

TABLE 4. Structual data on the local environment of Sb derived from the simulation of EXAFS data of synthesized tripuhyite and POIs in grain A

Sample	Shell	CN	*R* (Å)	ΔE_0 (eV)	σ^2 (Å^2)
tripuhyite syn.	Sb-O	6*	1.98 ± 0.01	4.40	0.003
	Sb-Fe_1	1.0*	3.07 ± 0.03	–	0.004
	Sb-Sb_1	1.0*	3.09 ± 0.03	–	0.006
	Sb-Fe_2	4.0*	3.62 ± 0.01	–	0.004
	Sb-Sb_2	4.0*	3.60 ± 0.02	–	0.006
	MS	8.0*	4.08 ± 0.03	–	0.007
spot 1	Sb-O	6.0	1.97 ± 0.01	4.01	0.004
	Sb-Fe_1	0.7 ± 0.4	3.06 ± 0.04	–	0.004
	Sb-Sb_1	0.2 ± 0.5	3.07 ± 0.03	–	0.006
	Sb-Fe_2	1.3 ± 0.7	3.59 ± 0.02	–	0.004
	Sb-Sb_2	1.6 ± 0.9	3.60 ± 0.03	–	0.006
	MS	3.2 ± 3.8	4.07 ± 0.03	–	0.008
spot 2	Sb-O	6.0	1.97 ± 0.01	4.81	0.003
	Sb-Fe_1	0.8 ± 0.5	3.07 ± 0.04	–	0.005
	Sb-Sb_1	0.8 ± 0.5	3.07 ± 0.03	–	0.005
	Sb-Fe_2	2.3 ± 0.8	3.60 ± 0.02	–	0.005
	Sb-Sb_2	1.4 ± 0.8	3.60 ± 0.03	–	0.005
	MS	4.0 ± 2.2	4.08 ± 0.03	–	0.008

Notes: CN = coordination number, *R* = interatomic distance, ΔE_0 = threshfold E_0 shift, and σ^2 = Debye-Waller factor. The estimated standard deviations in least-squares fit are given in parenthese and refer to the estimated error in the last decimal place.
* These values were fixed in the simulation.

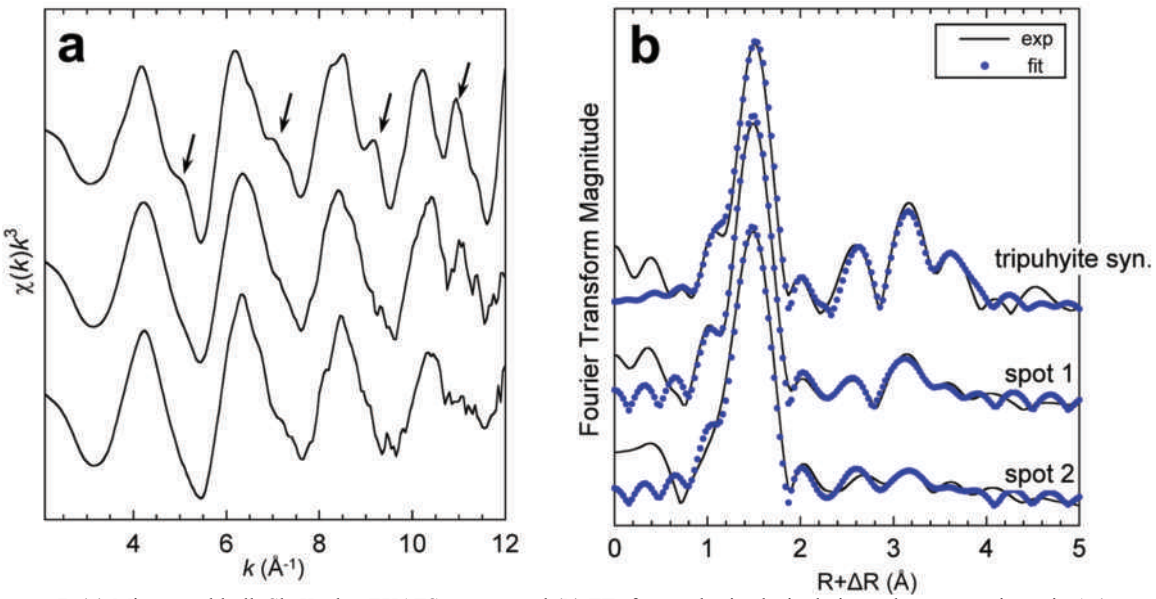

FIGURE 7. (**a**) Micro- and bulk Sb *K*-edge EXAFS spectra and (**b**) FTs for synthesized tripuhyite and two spots in grain A (spots 1 and 2 in Fig. 2a). The FT from *k* space to *r* space was performed in a range of 2.2–12.0 Å^{-1} for the three spectra. The arrows in **a** show the featured peaks observed in the spectrum of synthetic tripuhyite. (Color online.)

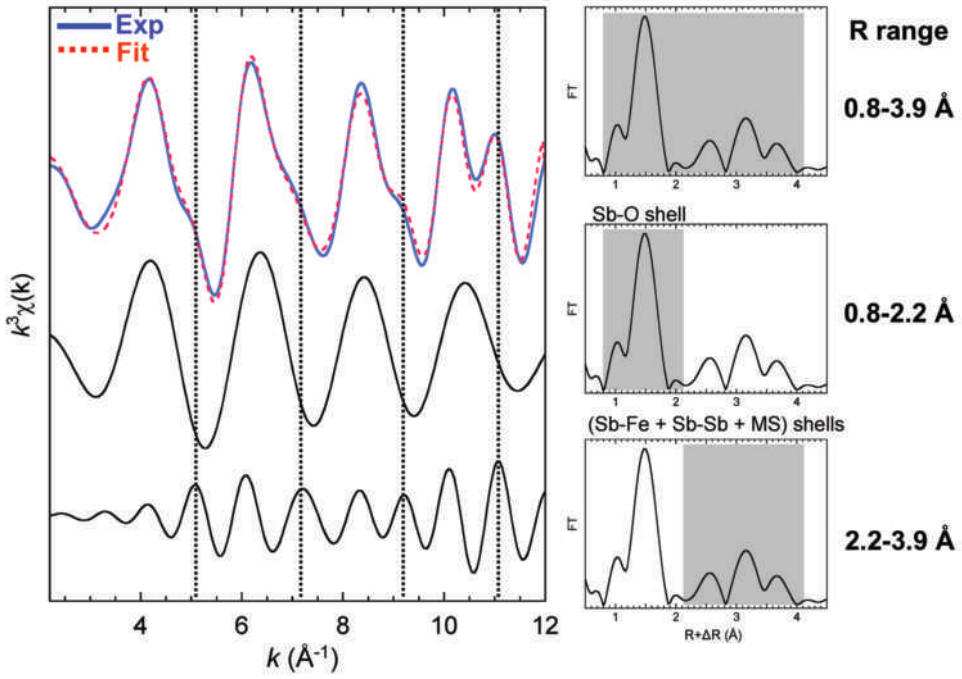

FIGURE 8. The upper spectra show the sum of Fourier filtered Sb-O, Sb-Fe, Sb-Sb, and MS contributions (blue line) with the theoretical spectrum (red dotted line) for the synthetic tripuhyite ($FeSbO_4$) sample. The middle and lower spectra show the Fourier filtered Sb-O and the other contributions (Sb-Fe, Sb-Sb, and MS), respectively. Black dotted bars represent the k of specific peaks observed in the experimental spectrum of the tripuhyite. (Color online.)

(2) multiple interatomic distances (structural disorder effect); and/or (3) over-absorption effects in the μ-EXAFS measurements. The decreased amplitude observed at Sb-Sb, Sb-Fe, and MS shells cannot arise from the over-absorption effect because the spectra of all spots in grain A were recorded in transmission mode and because this artifact would affect the Sb-O shell as well (Manceau et al. 2004, 2005), which is not seen in this case. Structural disorder in the solid increases as the particle size decreases, due most likely to the increasing proportion of surface-associated atoms (Waychunas et al. 2005). In fact, the μ-EXAFS modeled CNs in oxides often decrease in nanosized materials in comparison to bulk (Manceau et al. 2005; O'Loughlin et al. 2003). Therefore, we suggest that tripuhyite included in the Sb hot spots in grain A is nanoparticulate (scenario 1), and/or has high-structural disorder (scenario 2), which also agrees with the findings from μ-XRD.

TEM analyses

To obtain direct information on the particle size of the tripuhyite in grain A, we conducted TEM analyses of the soil aggregates detected from Sb hot spots in grain A (Fig. 9a). The TEM images show that the typical size of individual particles is around 10 nm. The size range of particles is uniform in parts of grain A. Electron diffraction was also measured at the area analyzed by TEM, and the diffraction pattern (shown as an inset in Fig. 9b) shows some diffuse rings, indicating the occurrence of nanoparticles or a highly disordered structure. The calculated *d*-spacings agree with those of published tripuhyite data (Berlepsch et al. 2003) [(110) 3.29 Å; (101) 2.57 Å; (211) 1.73 Å]. A similar finding was also observed in other parts of grain A. Thus, the formation of nanoparticulate tripuhyite in soil is confirmed by TEM analyses, which is consistent with particle size ranges suggested by μ-XRD and μ-EXAFS analyses. The small particle size leads to an increase in surface area associated with Sb and Fe atoms with respect to total atoms, which should cause the structural disorder in tripuhyite. The EDS spectrum (Fig. 9d) shows strong peaks of O, Fe, and Sb, which are also consistent with the presence of tripuhyite bearing these elements in grain A. The weak peaks of S, Al, Si, Mn, Cu, and As are also observed in the spectrum. The peaks are from detrital minerals in grain A and/or impurities incorporated into tripuhyite or ferrihydrite.

Implications of nanosized tripuhyite in natural soil

We studied soil grains collected from contaminated soil near Sb mine tailings and found a grain that has accumulated a much higher Sb content (40–60 wt% Sb_2O_5) than other grains. Detailed characterization by μ-XRD and μ-XAFS revealed that the grain is predominantly composed of ferric antimonate, tripuhyite ($FeSbO_4$). Moreover, characteristics of the Sb μ-EXAFS spectra are peculiar to nanoparticulate or disordered solid, and the particle size of tripuhyite is around 10 nm based on direct TEM analysis. This study is the first report showing the formation of tripuhyite and nanocrystallinity in natural soil to date.

Previous studies have indicated that nanosized Fe(III) oxides are formed by various inorganic pathways (e.g., oxidation of ferrous iron and neutralization of ferric iron in acid mine drainage) and/or biogenic pathways (e.g., ferrous iron oxidation by iron-oxidizing microorganisms) in aquatic environments (Banfield and Navrotsky 2001 and references therein). The lower solubility of Fe(III) relative to Fe(II) and faster oxidation kinetics due to higher pH lead to rapid precipitation of nanoscale Fe(III) hydroxides/oxides/oxyhydroxides (Banfield and Navrotsky; 2001). Thus, nanoparticles identified in the present study may have formed in a soil-water system through mechanisms similar to those mentioned above. Although previous studies of the mechanism of tripuhyite formation is very limited, one study did indicate that tripuhyite could be formed by precipitation from an aquatic phase based on synthesis experiments in laboratory (Scheinost et al. 2006).

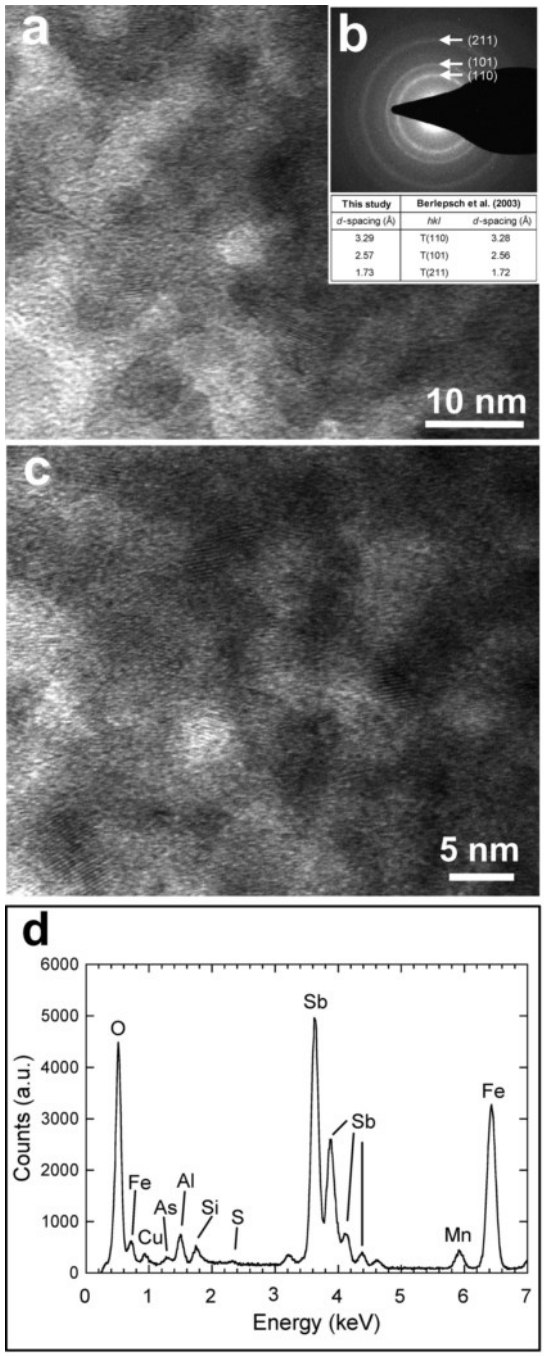

FIGURE 9. (**a** and **c**) TEM images of soil aggregates detected from grain A. (**b**) Electron diffraction pattern and (**d**) EDS spectrum of the area analyzed by TEM. The diffraction pattern matches the data of synthetic tripuhyite. The *d*-spacings values of the sample and reference (Berlepsch et al. 2003) are shown in the inset of **b**.

Mine wastewater steadily flowed from the mine-pits and tailings and into the soil investigated in this study. The wastewater contains high concentrations of both Sb and Fe (Sb: 2.2 mg/L, Fe: 0.2 mg/L, Fe/Sb ratio: 0.2) and is slightly acidified (pH 5–6). Since the soil water at the sampling site shows a slightly alkaline pH (pH 7.6 to 7.7), the formation of nanoparticulate tripuhyite in the present study may have involved direct precipitation by neutralization as a major process. In addition, the Si elemental map by EPMA shows that small silicate particles of less than 5 μm that are dispersed in grain A. This texture indicates that Fe hydroxides in the grain gradually grew by incorporating silicate particles during sedimentation (Ackermann et al. 2009). We speculate that tripuhyite in grain A may have formed in an aqueous system. If this process occurred, tripuhyite should be observed in several grains within the soil. However, tripuhyite was observed only in grain A and was not formed in other grains that have Fe/Sb ratios greater than 1. This implies that the formation of tripuhyite requires a threshold value of Fe/Sb ratio. Previous studies have reported that ferric arsenate and arsenical ferrihydrite gradually transform to nanosized scorodite ($FeAsO_4 \cdot 2H_2O$), indicating the solid as a precursor to scorodite formation (Jia et al. 2007; Paktunc et al. 2008). The transformation of ferric antimonite is also considered as a mechanism of tripuhyite formation in the present study. Paktunc et al. (2008) showed that when the initial Fe/As molar ratio increases, the solid predominantly transforms to two-line and six-line ferrihydrite, but not to scorodite. This suggests that the initial ratio of Fe/As strongly controls the formation of scorodite. These findings may explain why, in the present study, tripuhyite was observed in only one grain with an Fe/Sb = 1 (grain A), but not in other grains (grains B–D) with a higher Fe/Sb ratio; the threshold of tripuhyite formation is an Fe/Sb ratio greater than 1.

The discovery of tripuhyite in an aqueous environment may suggest the use of tripuhyite as a precipitation medium for Sb removal in contaminated environments by direct coprecipitation (such as scorodite for As). Addition of Fe hydroxides may lead to in situ formation of tripuhyite in soils and sediment. This study is a first step toward a better understanding of the formation of tripuhyite and Sb-bearing nanoparticles in aqueous systems. The physical and chemical properties of Sb-accumulated ferric oxides have been investigated to a limited extent (Scheinost et al. 2006; McComb et al. 2007; Mitsunobu et al. 2010). Even for tripuhyite, there is no available data for the solubility and stability for the bulk and nanoparticulate solids. Therefore, further research is needed involving both field and laboratory studies.

ACKNOWLEDGMENTS

We thank Y. Shibata and H. Ishisako for assistance in EPMA and thin section preparation, respectively. This work is partly supported by a fund from the University of Shizuoka. This work was performed with the approval of JASRI (Proposal Nos. 2008A1436, 2009A1243 2009A1571, and 2009B1575), Photon Factory (Proposal Nos. 2008G683 and 2009G655), and Advanced Light Source (Proposal No. ALS-02648).

REFERENCES CITED

Abreu, N.M. and Brearley, A.J. (2010) Early solar system processes recorded in the matrices of two highly pristine CR3 carbonaceous chondrites, MET 00426 and QUE 99177. Geochimica et Cosmochimica Acta, 74, 1146–1171.

Ackermann, S., Giere, R., Newville, M., and Majzlan, J. (2009) Antimony sinks in the weathering crust of bullets from Swiss shooting ranges. Science of the Total Environment, 407, 1669–1682.

Bancroft, P. (1988) Famous mineral localities: The Ichinokawa mine. The Mineralogical Record, 19, 229–238.

Banfield, J.F. and Navrotsky, A.. Eds. (2001) Nanoparticles and the Environment, vol. 44. Reviews in Mineralogy and Geochemistry, Mineralogical Society of America, Chantilly, Virginia.

Basso, R., Cabella, R., Lucchetti, G., Marescotti, P., and Martinelli, A. (2003) Structural studies on synthetic and natural Fe-Sb-oxides of MO_2 type. Neues Jahrbuch für Mineralogie-Monatshefte, 9, 407–420.

Berlepsch, P., Armbruster, T., Brugger, J., Criddle, A.J., and Graeser, S. (2003) Tripuhyite, $FeSbO_4$, revisited. Mineralogical Magazine, 67, 31–46.

Brannon, J.M. and Patrick, W.H. Jr. (1985) Fixation and mobilization of antimony in sediments. Environmental Pollution, 9, 107–126.
Casiot, C., Ujevic, M., Munoz, M., Seidel, J.L., and Elbaz-Poulichet, F. (2007) Antimony and arsenic mobility in a creek draining an antimony mine abandoned 85 years ago (upper Orb basin, France). Applied Geochemistry, 22, 788–798.
Chen, Y.-W., Deng, T.-L., Filella, M., and Belzile, N. (2003) Distribution and early diagenesis of antimony species in sediments and pore water of freshwater lakes. Environmental Science and Technology, 37, 1163–1168.
Crecelius, E.A., Bothner, M.H., and Carpenter, R. (1975) Geochemistries of arsenic, antimony, mercury, and related elements in sediments of Puget Sound. Environmental Science and Technology, 9, 325–333.
Endo, S., Terada, Y., Kato, Y., and Nakai, I. (2008) Chemical speciation of arsenic-accumulating mineral in a sedimentary iron deposit by synchrotron radiation multiple X-ray analytical techniques. Environmental Science and Technology, 42, 7152–7158.
Fandeur, D., Juillot, F., Morin, G., Olivi, L., Cognigni, A., Ambrosi, J.P., Guyot, F., and Fritsch, E. (2009) Synchrotron-based speciation of chromium in an Oxisol from New Caledonia: Importance of secondary Fe-oxyhydroxides. American Mineralogist, 94, 710–719.
Fawcett, S.E., Gordon, R.A., and Jamieson, H.E. (2009) Optimizing experimental design, overcoming challenges, and graining valuable information from the Sb *K*-edge XANES region. American Mineralogist, 94, 1377–1387.
Filella, M., Belzile, N., and Chen, Y.-W. (2002) Antimony in the environment: A review focused on natural waters II. Relevalent solution chemistry. Earth-Science Reviews, 59, 265–285.
Flynn, H.C., Meharg, A.A., and Bowyer, P.K. (2003) Antimony bioavailability in mine soils. Environmental Pollution, 124, 93–100.
Fuller, C.C., Davis, J.A., Waychunas, G.A. (1993) Surface chemistry of ferrihydrite: Part 2. Kinetics of arsenate adsorption and coprecipitation. Geochimica et Cosmochimica Acta, 57, 2271–2282.
Furuta, N., Iijima, A., Kambe, A., Sakai, K., and Sato, K. (2005) Concentrations, enrichment and predominant sources of Sb and other trace elements in size classified airborne particulate matter collected in Tokyo from 1995 to 2004. Journal of Environmental Monitoring, 7, 1155–1161.
Jia, Y., Xu, L., Wang, X., and Demopoulos, G.P. (2007) Infrared spectroscopic and X-ray diffraction characterization of the nature of adsorbed arsenate on ferrihydrite. Geochimica et Cosmochimica Acta, 71, 1643–1654.
Hammel, W., Steubing, L., and Debus, R. (1998) Assessment of the ecotoxic potential of soil contaminants by using a soil-algae test. Ecotoxicology Environmental Safety, 40, 173–176.
Hammersley, A.P. (1998) FIT2d V9.129, Reference manual V3.1; Vol. 346; ESRF internal report ESRF98HA01T. Macquarie University, Sydney.
He, M.C. and Yang, J.R. (1999) Effects of different forms of antimony on rice during the period of germination and growth and antimony concentration in rice tissue. Science Total Environment, 244, 149–155.
Kuperman, R.G., Checkai, R.T., Simini, M., Phillips, C.I., Speicher, J.A., and Barclift, D.J. (2006) Toxicity benchmarks for antimony, barium, and beryllium determined using reproduction endpoints for Folsomia candida, Eisenia fetida, and Enchytraeus crypticus. Environmental Toxicological Chemistry, 25, 754–762.
Krachler, M., Emons, H., and Zheng, J. (2001) Speciation of antimony for the 21st century: Promises and pitfalls. Trac-Trends in Analytical Chemistry, 20, 79–90.
Leuz, A.-K., Monch, H., and Johnson, C.A. (2006) Sorption of Sb(III) and Sb(V) to goethite: Influence on Sb(III) oxidation and mobilization. Environmental Science and Technology, 40, 7277–7282.
McComb, K.A., Graw, D., and McQuillan, A.J. (2007) ATR-IR spectroscopic study of antimonate adsorption to iron oxide. Langmuir, 23, 12125–12130.
Majzlan, J., Lalinska, B., Chovan, M., Jurkovic, L., Milovska, S., and Gottlicher, J. (2007) The formation, structure, and ageing of As-rich hydrous ferric oxide at the abandoned Sb deposit Pezinok. Geochimica et Cosmochimica Acta, 71, 4206–4220.
Manceau, A., Tamura, N., Marcus, M.A., MacDowell, A.A., Celestre, R.S., Sublett, R.E., Sposito, G., and Padmore, H.A. (2002) Deciphering Ni sequestration in soil ferromanganese nodules by combining X-ray fluorescence, absorption, and diffraction at micrometer scales of resolution. American Mineralogist, 87, 1494–1499.
Manceau, A., Marcus, M.A, Tamura, N., Proux, O., Geoffroy, N., and Lanson, B. (2004) Natural speciation of Zn at the micrometer scale in a clayey soil using X-ray fluorescence, absorption, and diffraction. Geochimica et Cosmochimica Acta, 68, 2467–2483.
Manceau, A., Tommaseo, C., Rihs, S., Geoffroy, N., Chateigner, D., Schlegel, M., Tisserand, D., Marcus, M.A., Tamura, N., and Chen, Z.S. (2005) Natural speciation of Mn, Ni, and Zn at the micrometer scale in a clayey paddy soil using X-ray fluorescence, absorption, and diffraction. Geochimica et Cosmochimica Acta, 69, 4007–4034.
Mitsunobu, S., Harada, T., and Takahashi, Y. (2006) Comparison of antimony behaviour with that of arsenic under various soil redox conditions. Environmental Science and Technology, 40, 7270–7276.
Mitsunobu, S., Takahashi, Y., Sakai, Y., and Inumaru, K. (2009) Interaction of synthetic sulfate green rust with antimony(V). Environmental Science and Technology, 43, 318–323.
Mitsunobu, S., Takahashi, Y., Terada, Y., and Sakata, M. (2010) Antimony(V) incorporation into synthetic ferrihydrite, goethite, and natural Fe oxyhydroxides. Environmental Science and Technology, 44, 3712–3718.
Murata, T., Kanao-Koshikawa, M., and Takamatsu, T. (2005) Effects of Pb, Cu, Sb, in and Ag contamination on the proliferation of soil bacterial colonies, soil dehydrogenase activity, andphospholipid fatty acid profiles of soil microbial communities. Water Air Soil Pollution, 164, 103–118.
O'Day, P.A., Rivera, N., Root, R., and Carroll, S.A. (2004) X-ray absorption spectroscopic study of Fe reference compounds for the analysis of natural sediments. American Mineralogist, 89, 572–585.
Oorts, K., Smolders, E., Degryse, F., Buekers, J., Gasco, G., Cornelis, G., and Mertens, J. (2008) Solubility and toxicity of antimony trioxide (Sb_2O_3) in soil. Environmental Science and Technology, 42, 4378–4383.
O'Loughlin, E.J., Kelly, S.D., Cook, R.E., Csencsits, R., and Kemmer, K.M. (2003) Reduction of uranium(VI) by mixed iron(II)/iron(III) hydroxide (green rust): Formation of UO_2 nanoparticles. Environmental Science and Technology, 37, 721–727.
Paktunc, D., Foster, A., and Laflamme, G. (2003) Speciation and characterization of arsenic in Ketza River mine tailings using X-ray absorption spectroscopy. Environmental Science and Technology, 37, 2067–2074.
Paktunc, D., Foster, A., Heald, S., and Laflamme, G. (2004) Speciation and characterization of arsenic in gold ores and cyanidation tailings using X-ray absorption spectroscopy. Geochimica et Cosmochimica Acta, 68, 969–983.
Paktunc, D., Dutrizac, J., and Gertsman, V. (2008) Synthesis and phase transformations involving scorodite ferric arsenate and arsenical ferrihydrite: Implications for arsenic mobility. Geochimica et Cosmochimica Acta, 72, 2649–2672.
Reguer, S., Dillmann, P., Mirambet, F., and Ballot-Gurlet, L. (2005) Local and structural characterization of chlorinated phases formed on ferrous archaeological artifacts by micro-XRD and micro-XANES. Nuclear Instruments and Methods in Physics Research Section B, 240, 500–504.
Scheinost, A.C., Rossberg, A., Vantelon, D., Xifra, I., Kretzschmar, R., Leuz, A.-K., Funke, H., and Johnson, C.A. (2006) Quantitative antimony speciation in shooting-range soils by EXAFS spectroscopy. Geochimica et Cosmochimica Acta, 70, 3299–3312.
Schwertmann, U. and Cornell, R.M. (2000) Iron oxides in the laboratory: Preparation and characterization. 2nd and extended ed. Wiley-VCH,Weinheim.
Suzuki, Y., Takeuchi, A., and Terada, Y. (2007) High-energy X-ray microbeam with total-refelection mirror optics. Review of Scientific Instruments, 78, 053713.
Takahashi, Y., Manceau, A., Geoffroy, N., Marcus, M.A., and Usui, A. (2007) Chemical and structural control of the partitioning of Co, Ce, and Pb in marine ferromanganese oxides. Geochimica et Cosmochimica Acta, 71, 984–1008.
Takaoka, M., Fukutani, S., Yamamoto, T., Horiuchi, M., Satta, N., Takeda, N., Oshita, K., Yoneda, M., Morisawa, S., and Tanaka, T. (2005) Determination of chemical form of antimony in contaminated soil around a smelter using X-ray absorption fine structure. Analytical Science, 21, 769–773.
Terada, Y., Goto, S., Takimoto, N., Takeshita, K., Yamazaki, H., Shimizu, Y., Takahashi, S., Ohashi, H., Furukawa, Y., Matsushita, T., and others. (2004) Construction and commissioning of BL37XU at SPring-8. AIP Conference Proceedings, 705, 376–379.
Thanabalasingam, P. and Pickering, W.F. (1990) Specific sorption of antimony(III) by the hydrous oxides of Mn, Fe, and Al. Water, Air, and Soil Pollution, 49, 175–185.
Utsunomiya, S., Kersting, A.B., and Ewing, R.C. (2009) Groundwater nanoparticles in the far-field at the Nevada test site: Mechanism for radionuclide transport. Environmental Science and Technology, 43, 1293–1298.
Warren, B.E. (1968) X-ray Diffraction, p. 381. Addison-Wesley, Reading, Massachusetts.
Waychunas, G.A. (2001) Structure, aggregation and characterization of nanoparticles. In J.F. Banfield and A. Navrotsky, Eds., Nanoparticles and the Environment, 44, p. 105–166. Reviews in Mineralogy and Geochemistry, Mineralogical Society of America, Chantilly, Virginia.
Waychunas, G.A., Kim, C.S., and Banfield, J.F. (2005) Nanoparticulate iron oxide minerals in soils and sediments: Unique properties and contaminant scavenging mechanisms. Journal of Nanoparticle Research, 7, 409–433.
Zabinsky, S.I., Rehr, J.J., Ankudinov, A., Albers, R.C., and Eller, M.J. (1995) Multiple-scattering calculations of X-ray-absorption spectra. Physical Review B, 52, 2995–3009.

MANUSCRIPT RECEIVED JULY 16, 2010
MANUSCRIPT ACCEPTED MARCH 21, 2011
MANUSCRIPT HANDLED BY BARRY BICKMORE